Direct sound speed measurements of MgO along planetary adiabats up to 400 GPa using shock-ramp compression

Hannah J. Bausch,[1,2,*] Joshua P. Townsend,[2,*] Jean-Paul Davis,[2] Sakun Duwal,[2] Christopher T. Seagle,[2] Tirzah M. Abbott,[1,3] Alisha N. Clark,[4] and Steven D. Jacobsen[4,†]

[1]*Department of Earth, Environmental, and Planetary Sciences, Northwestern University, Evanston, Illinois 60208, USA*

[2]*Sandia National Laboratories, Albuquerque, New Mexico 87185, USA*

[3]*NUANCE Center, Northwestern University, Evanston, Illinois 60208, USA*

[4]*Department of Earth Science, University of Colorado Boulder, Boulder, Colorado 80309, USA*

(Received 6 February 2026; revised 2 September 2026; accepted 14 October 2026; published 12 November 2026)

Accurate models of planetary formation and evolution rely on equation-of-state (EOS) models for their constituent materials across wide ranges of pressure, temperature, and density. Currently, estimates of thermoelastic properties along Earth-like pressure and temperature adiabats (the geotherm) require extrapolation of laboratory data, which confounds clear interpretation of the physical and chemical states of planetary interiors. We designed experiments on the Z Machine at Sandia National Laboratories to directly measure the EOS and sound speeds in dense oxides along quasi-isentropes close to the geotherm using shock-ramp compression. Here we demonstrate the method on magnesium oxide, representing the major nonsilicate mineral in the mantle, to pressures exceeding Earth's core. Our observations up to 400 GPa are confirmed by independent density functional theory and quantum Monte Carlo predictions and indicate the experimental compression path is close to a 1900 K geotherm. The results show excellent agreement with the preliminary reference Earth model (PREM), suggesting the technique can produce highly accurate thermoelastic data useful for interpreting the internal structure of terrestrial planets.

DOI: 10.1103/x7x6-16cs

I. INTRODUCTION

The internal structure and thermal evolution of planets are governed by the thermoelastic properties of their constituent materials [1,2]. On Earth, seismic measurements of acoustic waves provide constraints on the density, pressure, and physical state (solid or liquid) of the mantle and core [3]. Converting these data to a more detailed model of the physical and chemical structure of the Earth's interior is, however, much more difficult because it requires equation-of-state (EOS) data for all constituent materials [4,5]. Confounding this effort is the fact that laboratory measurements of sound velocity in minerals along planetary geotherm temperature profiles at pressures exceeding 100 GPa have not previously been attained by any method. When applied to Earth's lower mantle or to larger Super-Earth type planets, interior structure models rely on significant extrapolations of existing EOS and thermoelastic data [2]. Thus, an accurate understanding of the internal structure of the Earth and other planets is limited by the relatively large uncertainties in the thermoelastic properties of relevant materials at simultaneous high pressures and temperatures where executing experiments is challenging.

Periclase (MgO) is an endmember of ferropericlase (Mg,Fe)O, the most abundant nonsilicate oxide in Earth's mantle, as well as a primary standard material for developing new methods in high pressure science [6,7]. Previous experimental measurements of elastic properties such as the bulk sound speed have focused on static isothermal compression using diamond anvil cells and large volume presses, or conventional shock wave compression techniques [8–14]. Although these approaches can yield very precise measurements, interpretation of Earth's internal structure using these data can be complicated because the geotherm is approximately isentropic in the lower mantle [15].

The 'geotherm' is the set of adiabatic pressure-density-temperature states in Earth's mantle and is close to an isentrope away from thermal boundary layers [1]. Shock compression techniques probe a unique set of thermodynamic states known as a Hugoniot, which, while adiabatic, are not isentropic [16]. Thus, these conventional dynamic compression experiments in general do not probe geothermlike states [8,9,13,17]. More recently developed off-Hugoniot ramp compression techniques enable measurement of material properties along a nearly isentropic path, called a "quasi-isentrope" [18–28]. Previous ramp experiments on MgO have reported the pressure-density response and Lagrangian sound velocity along the principal isentrope [25,26], and more recent shock experiments have measured the sound speed in the liquid at elevated temperature [13,14], however the sound

*These authors contributed equally to this work.
†Contact author: steven.jacobsen@colorado.edu

Published by the American Physical Society under the terms of the Creative Commons Attribution 4.0 International license. Further distribution of this work must maintain attribution to the author(s) and the published article's title, journal citation, and DOI.

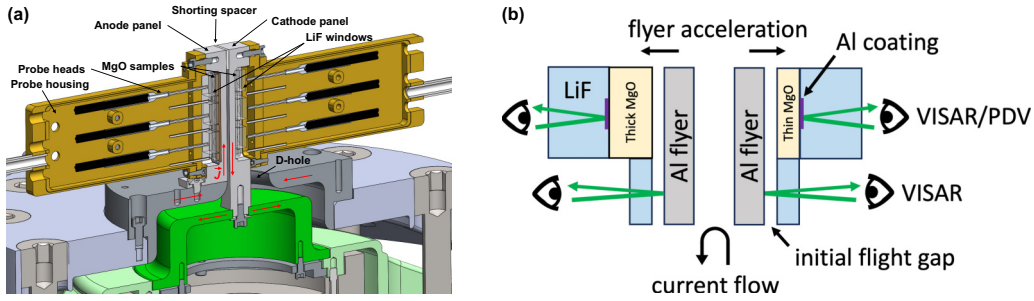


FIG. 1. (a) Hardware rendering for shot Z3809 target assembly. Red arrows show the current (J) path, after [39]. (b) Schematic of the sample assembly and probe setup. A photograph of the cathode panel is shown in Fig. S2 along with a description of the target hardware.

speed along a geothermlike path has not yet been measured [25,26].

In this study, we measured the sound speed of polycrystalline MgO along an approximate geotherm up to 400 GPa by means of shock-ramp dynamic compression experiments on the Z Machine at Sandia National Laboratories. The experimental results show excellent agreement with independent density functional theory and quantum Monte Carlo predictions and indicate that the experimental compression path is close to a 1900 K geotherm. We demonstrate that these techniques can produce highly accurate, absolute EOS data useful for interpreting the internal structure of terrestrial planets.

II. SHOCK-RAMP EXPERIMENTS

The Z Machine (Z) is a pulse-power facility capable of storing ∼25 MJ of stored electrical energy and delivers ∼2 MJ of that energy to a cm-scale target in a submicrosecond time scale [29]. Shock-ramp experiments make use of a planar stripline target (Figs. 1 and S2) and a double-ramp pulse shape (Fig. S2) [18,19,30]. A combination of 1-D and 2-D magnetohydrodynamic codes and a transmission-line circuit model of Z were used to determine both the electrical-current pulse shape required to generate the shock-ramp compressions of samples and the appropriate Z Machine configuration needed to produce that pulse shape [29]. In the present work, the first ramp accelerated an Al flyer across a gap, impacting the sample to generate a shocked state on its Hugoniot curve at ∼110 or ∼140 GPa (shots Z3809 and Z3866, respectively). Then the remaining energy in the second ramp further ramp-compressed the sample to at least 400 GPa.

The Hugoniot curve of single-crystal MgO ($\rho_0 = 3.58\,\mathrm{g/cm^3}$) intersects pressures relevant to Earth's mantle at temperatures well below the geotherm. For example, current estimates, poorly constrained, put the temperature at Earth's CMB (135 GPa) at approximately 2600 K [31–33], whereas at 135 GPa the Hugoniot curve of single-crystal MgO is at a temperature of ∼1900 K [34]. Polycrystalline samples with porosity and lower density, however, have higher Hugoniot temperatures than single-crystal (fully dense) MgO at the same pressures, allowing a shock directly to the geotherm at lower-mantle pressures. We found that polycrystalline MgO with ∼7% porosity ($\rho_0 = 3.33\,\mathrm{g/cm^3}$) shocked to approximately 110 GPa followed by subsequent ramp compression probes a quasi-isentrope close to a 1900 K geotherm [4,15,35], motivating the synthesis of high-quality polycrystalline MgO samples.

Magnesium oxide powder was hot-pressed in Ar to 20 MPa and 1000 °C at American Isostatic Presses Inc. After HP-HT treatment, individual samples for experiments were prepared by cutting and polishing samples to size, approximately 7 × 8 mm across and of variable thickness (0.8–1.2 mm). Density of individual samples was measured by the Archimedes method and found to range from 3.31–3.41 g/cm^3. Further details of sample preparation and characterization are provided in the Supplemental Material (Table S1, Fig. S1) [36].

The experimental configuration consisted of measuring particle velocities in a pair of samples with different thicknesses positioned at the same height on the two electrode panels of a stripline [Fig. 1(a)]. Different sample thicknesses allow us to measure the time difference for the compression wave to propagate through the sample, thereby providing a direct measure of the sound speed. Polycrystalline MgO samples were backed by 2.5-mm thick single crystal [100] lithium fluoride (LiF) windows and tacked onto a shelf 0.785 mm (Z3809) or 0.970 mm (Z3866) above the 2.3-mm thick electrode floor, setting the flight gap [Fig. 1(b)]. LiF windows were coated at the sample-window interface with 2500 Å of aluminum over a 3-mm diameter central spot to provide a specular reflector for laser-based velocimetry measurements. Both a velocity interferometer system for any reflector (VISAR) [37] and a photon Doppler velocimetry (PDV) system [38] were used to measure particle velocities, u_p, at each sample-LiF interface as a function of time.

The averaged particle velocity of the transmitted waveform in the window for both thick and thin samples measured by velocimetry are shown in Fig. 2. It is important to note that the shock states from which the thin and thick samples are ramp compressed are slightly different. In both experiments (Z3809 and Z3866), the incident shock pressure in the thicker samples is slightly higher than in the thinner samples, which we attribute to shock growth. The difference in shock pressure was less than 3.5%, so we averaged the shock pressure between the thick and thin samples for subsequent analysis. The Lagrangian wave velocity, c_L, as a function of compression velocity, u^* (defined as the velocity attained under compression by a simple, unidirectional noninteracting wave), was obtained through inverse Lagrangian analysis of u_p measured at the interface, as discussed in previous works [18,22,39–41]; particularities specific to the present work are discussed in Sec. IV.

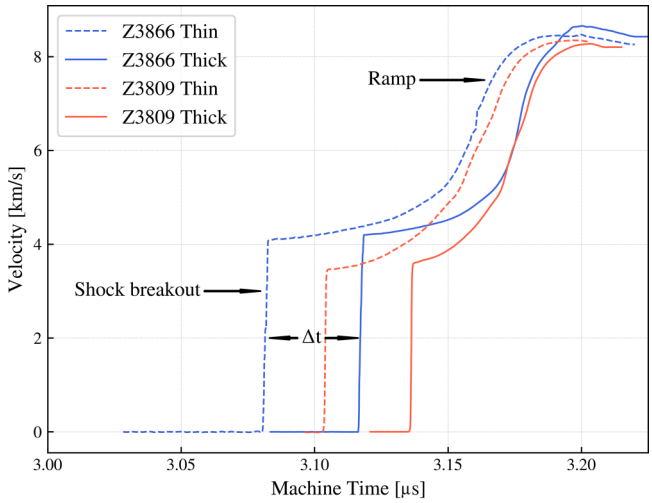


FIG. 2. Averaged PDV velocimetry from Z3866 (blue) and averaged PDV and VISAR velocimetry from Z3809 (red). The 'thin' samples (dashed lines) and 'thick' samples (solid lines) are positioned on opposite sides of the stripline at the same elevation (Fig. 1). The difference in the measured times when the thick and thin samples have reached the same particle velocity gives an estimate of the Lagrangian sound velocity, from which thermoelastic response and bulk sound speed are obtained. Note that the shock growth is apparent with the transmitted-shock particle velocities of the thick samples being slightly higher than the corresponding thin samples.

III. *AB INITIO* CALCULATIONS

To provide a point of comparison to the unique loading path of the experiments, we carried out complementary *ab initio* equation-of-state calculations. Density functional theory based molecular dynamics (DFTMD) calculations were performed using VASP (version 6.3.2), an implementation of Kohn-Sham density functional theory with periodic boundary conditions and a plane wave basis [42–44]. The exchange and correlation energies were obtained from the generalized gradient approximation of Perdew, Burke, and Ernzerhof (PBE) [45]. All VASP calculations employed a 216-atom supercell of B1 MgO and used PAW pseudopotentials with a 800-eV plane-wave energy cutoff and $2s^2 2p^6 3s^2$ and $2s^2 2p^4$ valences for Mg and O, respectively [46–48]. The Brillouin zone was sampled at k = (¼, ¼, ¼) and the Mermin functional was used to set electronic occupations [49]. Typical simulations were run for 10 000 1-fs timesteps and from which the average energy and pressure were calculated on a grid of densities spanning 3.2–7.0 g/cm^3 with a 0.2 g/cm^3 spacing and temperatures of 300, 500, 1000, 2000, 3000, and 4000 K. We also computed the equation of state of the static lattice (cold curve) using the same computational parameters on the same density grid that was used in the MD calculations. As expected, the PBE bulk modulus is lower than, and the reference volume is higher than, the estimated values extrapolated down to 0 K from experimental measurements, as shown in Table I.

To improve the static equation of state, we carried out real-space diffusion Monte Carlo calculations on the same density grid using the QMCPACK code (version 3.17.1) [51,52]. These calculations require as input a set of DFT orbitals

TABLE I. Comparison of Vinet equation-of-state parameters obtained from our DFT and DMC calculations and previous experimental measurements [50]. Details of extrapolated estimates of the experimental EOS parameters to 0 K are given in the Supplemental Material [36].

	B_0 / GPa	B_0'	V_0 / Bohr^3/f.u.
Expt. (Fei 1999 300 K)	160(2)	4.15 (Fixed)	126.18
Expt. (Fei 1999 0 K)	169(3)	4.15 (Fixed)	124.99(5)
DFT / PBE (300 K)	141.0(3)	4.58 (1)	130.18(3)
DFT / PBE (0 K)	148 (1)	4.48(3)	129.45(9)
DMC (300 K)	168.1(3)	4.46 (1)	123.77(2)
DMC (0 K)	174 (1)	4.37(3)	123.31(9)

which were obtained using QUANTUM ESPRESSO (version 7.3) [53,54]. The exchange and correlation energies were obtained from PBE [45]. For both DFT and QMC calculations, we used "correlation consistent" effective core potentials specifically constructed to enable highly accurate QMC calculations [55,56]. Following previous work [51,52], the calculations assumed a Slater-Jastrow trial wave function with optimized one-, two-, and three-body Jastrow factors. Twist-averaged estimates of the total energies were obtained from fixed-node DMC calculations on 216 atom supercells sampled with four k-points on the same density grid that was used for the DFTMD EOS calculations. We used the size-consistent 'T-moves' scheme of Casula *et al.* to ensure variational sampling of the nonlocal pseudopotential term [57]. The DMC algorithm relies on a Trotter decomposition of the imaginary time evolution operator and therefore suffers from a time step error. Our DMC calculations were performed with timesteps of 0.064, 0.016, 0.008, 0.004, and 0.002 Ha^{-1} from which zero timestep estimates were obtained from a least-squares fit to a quadratic polynomial. The resulting static equation of state obtained from a fit of the DMC total energy to a Vinet equation of state shows a substantial improvement over the DFT/PBE results, as shown in Table I.

To correct the DFTMD data at finite temperatures we note that the total energy, E, and pressure, P, can be expressed as a sum of two terms:

$$E^{\mathrm{DFTMD}}(V,T) = E_0^{\mathrm{DFT}}(V) + E_{\mathrm{th}}^{\mathrm{DFTMD}}(V,T) \quad (1)$$

$$P^{\mathrm{DFTMD}}(V,T) = P_0^{\mathrm{DFT}}(V) + P_{\mathrm{th}}^{\mathrm{DFTMD}}(V,T)\,, \quad (2)$$

where V is the volume, T temperature, the subscript 0 indicates the 'cold curve', and the subscript 'th' indicates the thermal contribution due to the motion of the atoms and electronic excitations. With these expressions in mind, we corrected the finite temperature DFTMD results with the static DMC equation of state (referred to hereafter as the "QMC-corrected" equation of state) according to

$$\begin{aligned} E^{\mathrm{corr}}(V,T) &= E^{\mathrm{DFTMD}}(V,T) + E_0^{\mathrm{DMC}}(V) - E_0^{\mathrm{DFT}}(V) \\ &= E_0^{\mathrm{DMC}}(V) + E_{\mathrm{th}}^{\mathrm{DFTMD}}(V,T). \end{aligned} \quad (3)$$

In both DFT and DMC the cold-curve energy and pressure were obtained from Vinet EOS fits to the energy. The pressure was obtained self-consistently from the fit of the energy EOS

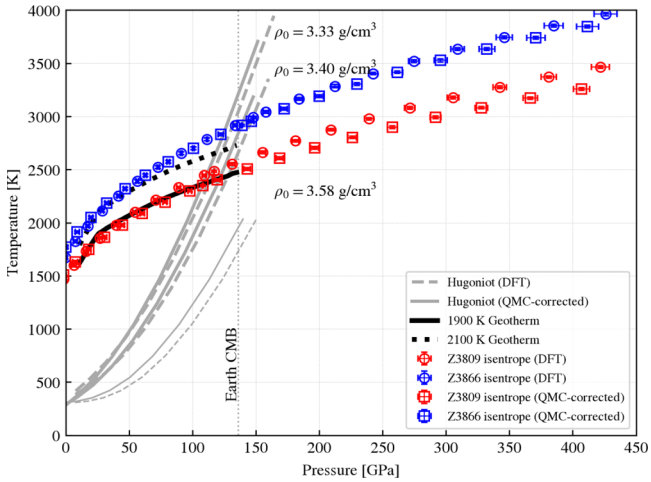


FIG. 3. Predicted quasi-isentropes corresponding to Z3809 (red) and Z3866 (blue) obtained from DFTMD (circles) and QMC-corrected (squares) EOS models. Hugoniot curves for various initial densities shown in gray, with DFT (QMC-corrected) predictions shown in dashed (solid) lines. Geotherms from [15] shown in black. Earth's core-mantle boundary is denoted with a thin vertical dotted line.

from the definition:

$$P_0 \equiv -\left(\frac{\partial F}{\partial V}\right)_{T=0} = -\left(\frac{\partial E_0}{\partial V}\right). \tag{5}$$

In DFTMD and QMC, one obtains only a statistical estimate of the energy. Our QMC-corrected equation of state includes the statistical uncertainties in both energy and pressure obtained from DFTMD as well as those from the DMC calculations. Thus, the QMC-corrected EOS has strictly larger statistical uncertainties than those of the original DFTMD EOS. The uncertainty in the DMC estimate of the energy is straightforwardly estimated from the calculations but uncertainties in the DMC pressures were obtained from a bootstrap resampling procedure in which the energies were varied according to their uncertainties and then fit to a Vinet equation of state 1000 times from which average and standard deviation were calculated.

The principal Hugoniot states were computed in the usual way following previous work [24,58–61] and are shown in Fig. 3. The ramp states were estimated by the following procedure: Taking as an initial state the incident-shock state corresponding to the measured particle velocity from the experiments, we then compute the shock state using the closest density grid points (above and below the shock state). Then the reference point is updated to be this state and the process is repeated, moving up and down in density to obtain the rest of the isentrope. This 'sequence of shocks' approximation is exact in the limit of infinitesimal density change, but in practice necessarily results in a small (systematic) error in the isentrope thus obtained. We found that a density step size of 0.2 g/cm^3 provided converged estimates of the pressure, temperature, energy, and sound speed along the approximate isentrope for the states considered here (Fig. S9).

By design, these calculations capture only the equilibrium response of the material and therefore do not account for material strength or other strain rate dependent effects. Overall, we find that the incorporation of QMC corrections to the EOS modifies the density and compressibility under both static (0 K) and finite temperature conditions. This effect is clearly observed in both the Hugoniot curve and isentrope calculations, shown in Fig. 3. Matching to the experimentally observed incident-shock state in the sample, QMC-corrected calculations result in incident-shock states with lower pressure, less density, and lower temperature than DFTMD calculations, and are closer to the experimental result (Table II). These differences are also reflected in the isentrope calculations, which show that the QMC-corrected EOS model tends to predict lower temperatures than the DFTMD EOS model at high pressures. Interestingly, the QMC-corrected EOS suggests that the experimental loading paths for Z3809 and Z3866 are very close to 1900 and 2100 K geotherms, respectively [15]. The DFTMD data, DMC corrections, principal Hugoniot states, and shock-ramp states are given in the Supplemental Material [36].

IV. RESULTS

From the measured window-interface velocity histories we determined the Lagrangian sound velocity c_L along the postshock compression ramp using an inverse Lagrangian analysis (ILA) method [28]. In contrast to ramp-only compression where the ambient state is accurately known, in our shock-ramp experiments the take-off state, or incident-shock state, for the ramp is initially unknown, although it must lie on the principal Hugoniot. Building on previous work [9,16,28,50], we generalized our ILA method to handle an initial guess of an EOS from which we then iteratively solve for a compression curve that starts from a state on the principal Hugoniot and is consistent with the measured velocities. The incident-shock states in experiments were determined from assumed shock Hugoniots. We used experimental data from the LASL handbook for MgO with $\rho_0 = 3.34\,\mathrm{g/cm^3}$ to determine the incident-shock state for Z3809 ($\rho_0 = 3.33\,\mathrm{g/cm^3}$). For this experiment, the QMC-corrected pressure and density agree to within 3 GPa and 0.03 g/cm^3, respectively, at the incident-shock state, as shown in Table II. Given the agreement observed between experiment and QMC-corrected theory along the Hugoniot, and due to the lack of experimental principal Hugoniot data available for MgO with $\rho_0 = 3.40\,\mathrm{g/cm^3}$, we used our QMC-corrected principal Hugoniot to determine the incident-shock state u_p for Z3866 ($\rho_0 = 3.40\,\mathrm{g/cm^3}$). For Z3866, because the known incident-shock state was assumed from QMC, the incident-shock state for the ramp was the same for both experiment and calculations.

The ILA results for Lagrangian sound velocity as a function of compression velocity are shown as dots in Fig. 4, with the shaded region indicating statistical uncertainty obtained from a bootstrap analysis of the velocimetry data. We attribute the initial decrease of measured c_L at the beginning of the ramp to a transition from elastic to inelastic deformation, suggesting that when the ramp compression arrives, the postshock stress state in the solid is no longer at a compressive elastic limit (e.g., yield-stress surface); the initially longitudinal sound speed falls to a bulk sound speed after the transition [22,39]. The deviatoric stress increment given by integrating

TABLE II. Incident-shock states at the start of ramps for shots Z3809 and Z3866.

	P/GPa	ρ_0/ g/cm^3	T/K
Shot Z3809: $\rho_0 = 3.33$ g/cm^3, $u_p = 3.268$ km/s			
Experiment	110.8(6)	4.909(11)	-
QMC-corrected	108.1(3)	4.897	2342(8)
DFTMD	117.0(1)	4.874	2475(10)
Shot Z3866: $\rho_0 = 3.4$ g/cm^3, $u_p = 3.763$ km/s			
Experiment and QMC-corrected	139.1(4)	5.141	2903(9)
DFTMD	148.1(1)	5.121	2978(10)

the difference between measured c_L and extrapolated bulk Lagrangian sound speed across this transition is approximately 6 GPa, which compares favorably with previous measurements made at 40 GPa that found a yield strength of ∼4 GPa [17,62]. Unlike previous works using ILA to analyze data from ramp or shock-ramp experiments, we replace each $c_L(u^*)$ curve with a linear fit to the data, excluding the elastic-inelastic transition region; these are shown by thick lines in Fig. 4, with dotted lines showing extrapolation down to the incident-shock state. Setting c_L to be linear in u^* effectively assumes pressure is second order in strain. This approach introduces a model-based constraint to our experimental result, but insofar as the material's real behavior across the probed range of compression can be described by a low-order compression curve, it also serves to remove the effects of nonideal phenomena like the elastic-plastic transition described above. Best-fit parameter values for the linear $c_L(u^*)$ model are reported in Table III.

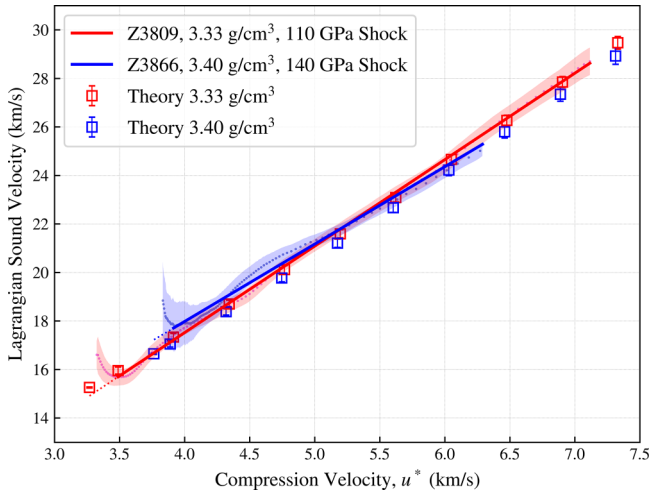


FIG. 4. Lagrangian sound velocity obtained from ILA along the ramp from initial shock states of 110 and 140 GPa for shots Z3809 (red) and Z3866 (blue), respectively. Velocities obtained from ILA are shown as points, shaded areas represent experimental uncertainty [39], and thick lines show the linear fits from Table III. For clarity, the data density shown as points is reduced but the complete c_L-u^* dataset is available in the Supplemental Material [36]. Linear fits are fitted to data within the compression velocity range of the thick lines. The linear fits are extrapolated back to the Hugoniot state and are represented by dotted lines. Red and blue open squares denote QMC-corrected predictions.

Corresponding stress-density states along each quasi-isentrope were obtained from the linear fits via Eqs. (6) and (7) (compare with Eqs. (4) and (5) from Ref. [39] which use different integration limits), where u_H^* is the compression velocity at the incident shock state and σ_x is longitudinal stress:

$$\sigma_x = \rho_0 \int_{u_H^*}^{u^*} \mathrm{d}u \, c_L(u) \tag{6}$$

$$\rho = \rho_0 \left[1 - \int_{u_H^*}^{u^*} \frac{\mathrm{d}u}{c_L(u)} \right]^{-1}. \tag{7}$$

We have assumed that c_L is equal to the Lagrangian bulk sound velocity, neglecting thermal pressure due to entropy-generating mechanisms (e.g., inelastic deformation) and elastic-limit hardening. Detailed accounting for all strength effects would require a pressure, temperature, and strain-rate dependent strength model which at present does not exist for MgO, and the development thereof would constitute a significant undertaking well outside the scope of the present work [63]. We therefore proceed under the assumption that $\sigma_x \approx P$ in Eq. (6).

The pressure-density states obtained from our shock-ramp experiments are shown in Fig. 5. Because the starting density of our MgO samples was substantially lower than that of a fully dense single crystal (3.33 or 3.40 g/cm^3 vs 3.58 g/cm^3), we have normalized the densities shown in Fig. 5 by their respective starting density. This more clearly shows the change in compressibility due to differences in the initial state and loading path. For comparison, pressure-density states where density is not normalized are shown in Fig. S3. Due to the unique loading paths of our experiments, the pressure-density states obtained are significantly different from previous dynamic compression studies. The data from Root *et al.* [34], Vassiliou and Ahrens [64], and the LASL Handbook [65] lie along the principal Hugoniot obtained from fully dense samples, whereas the data from Coppari *et al.* [25] correspond to the principal quasi-isentrope [34,64,65].

TABLE III. Best fit parameters for the c_L-u^* ramp measurements. $c_L(u^*) = mu^* + b$.

	Z3809	Z3866
m	3.546(6)	3.19(2)
b	3.35(3)	5.20(9)

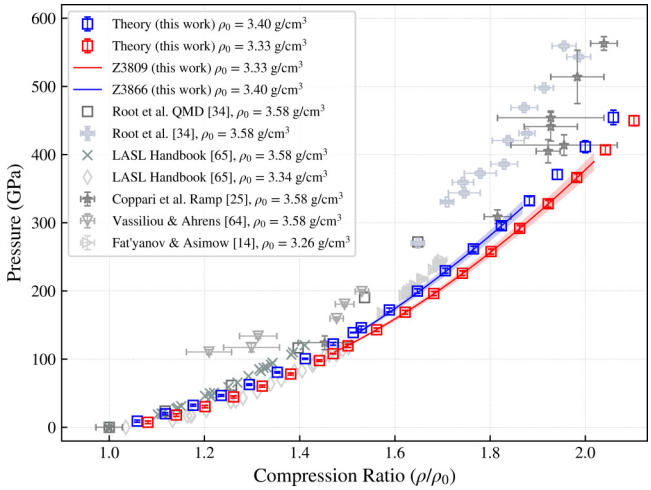


FIG. 5. Comparison of pressure-density states along various loading paths. Shaded areas represent experimental uncertainty. The data from Root *et al.* [34], the LASL handbook (Marsh [65]), and Vassiliou and Ahrens [64] lie along a common shock Hugoniot curve while the data from Coppari *et al.* [25] follow along the principal quasi-isentrope of the fully dense crystal [25,34,64,65]. Additionally, data from the LASL handbook includes a separate shock Hugoniot curve from porous samples with a density of 3.34 g/cm^3. The data from Fat'yanov and Asimow [14] lie along a shock Hugoniot curve from samples preheated to ∼2300 K and correspond to the liquid state [14]. Red and blue points denote QMC-corrected DFTMD predictions of the experimental ramp.

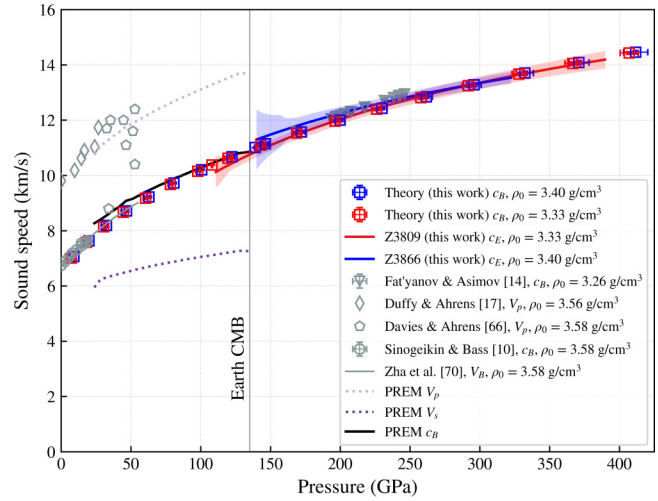


FIG. 6. Measured Eulerian sound speed on quasi-isentropes compared to previous measurements and PREM [3]. Shaded areas represent associated experimental uncertainty. Note that the points obtained by Fat'yanov and Asimow [14] correspond to liquid MgO [14]. The experiments by Duffy and Ahrens [17], Davies and Ahrens [66], and Zha *et al.* [70] measured longitudinal wave speed (V_P). Red and blue points denote QMC-corrected DFTMD predictions.

As expected, principal Hugoniot data show a lower compressibility than either the experimental ramp data of Coppari *et al.* [25] or our experimental shock-ramp data. For example, Root *et al.* [34] show a compression ratio 12% lower than the compression ratio reached on shock-ramp path to a pressure of 270 GPa. Our QMC-corrected EOS model shows excellent agreement with the experimentally measured pressure-density states for Z3809. Near 363 GPa, the experimental density is 6.65 g/cm^3 while the DFTMD predicted density is 6.45 g/cm^3. The QMC-corrected density is 6.60 g/cm^3; much improved over the DFT estimate and within 1% of the experimental value. The excellent agreement between experiment and theory suggests that strength effects are likely small in the experiments.

To obtain experimental sound speeds, the Eulerian sound velocity, c_E, is obtained via Eq. (8), where ρ is the density along the ramp, and the subscript 0 denotes the value in the uncompressed initial state. Uncertainty was propagated in quadrature.

$$c_E = c_L \frac{\rho_0}{\rho}. \tag{8}$$

Figure 6 shows sound speeds as a function of pressure. For a solid undergoing uniaxial deformation with fully inelastic deviatoric component (and ignoring thermal pressure from dissipation), the longitudinal Eulerian wave speed is equivalent to the bulk sound speed, $c_B = \sqrt{K_S/\rho}$, geophysically relevant because c_B can be obtained in the deep Earth from observed teleseismic travel times and normal modes of oscillation [3]. Because the bulk sound speed is relatively insensitive to temperature in these regimes, we found that the Eulerian velocities obtained from Z3809 and Z3866 are nearly indistinguishable, despite the difference in ramp take-off points. The predicted bulk sound speed obtained from the QMC-corrected EOS model lies within error of our measurements. Generally, we find excellent agreement with previous measurements obtained from both static and dynamic compression experiments where available.

The data from Fat'yanov and Asimow [14] are from gas-gun experiments on preheated samples and thus probed high-temperature liquid states. The experiments by Davies and Ahrens [66] measured longitudinal acoustic wave velocity and the transition from elastic to inelastic deformation around 50 GPa, which resulted in a marked reduction in the velocity [66].

The quasi-isentropes corresponding to Z3809 and Z3866 are close to lower mantle geotherms and therefore provide a direct measurement of the elastic properties of solid MgO in real lower mantle pressure and temperature conditions. We find that the bulk sound speed is essentially indistinguishable from the predicted Preliminary Reference Earth Model (PREM) value, which is surprising and potentially coincidental because the PREM values are representative of a chemically complex multicomponent assemblage [3]. While not intended to make any direct implication about Earth's mantle mineralogy or temperature, we compared our sound velocity measurements of MgO along 1900 K and 2100 K adiabats to PREM only as a way to visualize that the new methodology produces results consistent with what is expected for a planetary interior.

V. CONCLUSIONS

Obtaining high precision equation-of-state measurements at pressure and temperature regimes relevant for planetary

interiors remains a significant challenge. We performed experiments on MgO that follow isentropes close to Earth's geotherm by designing dual-sample stripline loads and predictively pulse-shaping the current on Z to ramp compress the samples from a shocked state using magnetic pressure. Complementary *ab initio* modeling, including highly accurate quantum Monte Carlo corrections to the static equation of state, show excellent agreement with the experimental data and demonstrate the importance of similar methods for related problems.

Although the temperature was not directly measured, the remarkable agreement between the experimental and predicted shock-ramp states suggests both that entropy contributions due to irreversible processes such as changes in microstructure and inelastic deformations in general are not significant in our experiments and that the measured ramp states are close to geotherm temperatures in Earth's lower mantle. Although Z3809 and Z3866 probe distinct thermodynamic states, we find the bulk sound speed is relatively insensitive to the shock state from which the ramp proceeds due to the competing effects of pressure and temperature. Our results represent the first measurements of bulk sound speed of a geomaterial along realistic lower mantle adiabats and the experimental techniques and results presented here will be useful for future studies of the B1-B2 phase transition at high temperatures and for improving models of the interior structure of the Earth and terrestrial exoplanets.

ACKNOWLEDGMENTS

Experimental time at the Z facility was provided through the Z Fundamental Science Program to S.D.J. This work was supported by the DOE-NNSA Cooperative Agreement No. DE-NA0003975 to the Chicago/DOE Alliance Center (CDAC). Sandia National Laboratories is a multimission laboratory managed and operated by National Technology and Engineering Solutions of Sandia, a wholly owned subsidiary of Honeywell International, for the U.S. Department of Energy's National Nuclear Security Administration (DOE/NNSA) under Contract No. DE-NA0003525. We thank the teams at Sandia National Laboratories for target fabrication and the operation of the Z facility. This paper describes objective technical results and analysis. Any subjective views or opinions that might be expressed in the paper do not necessarily represent the views of the U.S. Department of Energy or the U.S. Government. This research was supported in part through the computational resources and staff contributions provided for the Quest high-performance computing facility at Northwestern University, which is jointly supported by the Office of the Provost, the Office for Research, and Northwestern University Information Technology. This work made use of the EPIC facility (RRID: SCR_026361) of Northwestern University's NUANCE Center, which has received support from the IIN and Northwestern's MRSEC program (NSF DMR-2308691).

S.D.J. and J.P.T. conceived the project. H.J.B., J.-P.D., S.D., and S.D.J. conducted the experiments. C.T.S. and J.-P.D. supported experimental design and data analysis. H.J.B. and J.P.T. carried out calculations. H.J.B. synthesized and fabricated samples. T.M.A. carried out SEM and EBSD sample preparation and analysis. All authors contributed equally to conceptualization and writing.

DATA AVAILABILITY

The data that support the findings of this article are openly available [67].

[1] W. Lowrie and A. Fichtner, *Fundamentals of Geophysics*, 2nd ed. (Cambridge University Press, Cambridge, 2020).

[2] D. Valencia, R. J. O'Connell, and D. Sasselov, Internal structure of massive terrestrial planets, Icarus **181**, 545 (2006).

[3] A. M. Dziewonski and D. L. Anderson, Preliminary reference Earth model, Phys. Earth Planet. Inter. **25**, 297 (1981).

[4] W. Xu, C. Lithgow-Bertelloni, L. Stixrude, and J. Ritsema, The effect of bulk composition and temperature on mantle seismic structure, Earth Planet. Sci. Lett. **275**, 70 (2008).

[5] F. Wang, M. Barklage, X. Lou, S. van der Lee, C. R. Bina, and S. D. Jacobsen, HyMaTZ: A python program for modeling seismic velocities in hydrous regions of the mantle transition zone, Geochem. Geophys. Geosyst. **19**, 2308 (2018).

[6] S. D. Jacobsen, C. M. Holl, K. A. Adams, R. A. Fischer, E. S. Martin, C. R. Bina, J.-F. Lin, V. B. Prakapenka, A. Kubo, and P. Dera, Compression of single-crystal magnesium oxide to 118 GPa and a ruby pressure gauge for helium pressure media, Am. Mineral. **93**, 1823 (2008).

[7] F. V. Kaminsky, *The Earth's Lower Mantle* (Springer International Publishing, Cham, 2017).

[8] O. V. Fat'yanov, P. D. Asimow, and T. J. Ahrens, Thermodynamically complete equation of state of MgO from true radiative shock temperature measurements on samples preheated to 1850 K, Phys. Rev. B **97**, 024106 (2018).

[9] T. S. Duffy, R. J. Hemley, and H. Mao, Equation of state and shear strength at multimegabar pressures: Magnesium oxide to 227 GPa, Phys. Rev. Lett. **74**, 1371 (1995).

[10] S. V. Sinogeikin and J. D. Bass, Single-crystal elasticity of pyrope and MgO to 20 GPa by Brillouin scattering in the diamond cell, Phys. Earth Planet. Inter. **120**, 43 (2000).

[11] S. Speziale, C. Zha, T. S. Duffy, R. J. Hemley, and H. Mao, Quasi-hydrostatic compression of magnesium oxide to 52 GPa: Implications for the pressure-volume-temperature equation of state, J. Geophys. Res. **106**, 515 (2001).

[12] A. E. Gleason, H. Marquardt, B. Chen, S. Speziale, J. Wu, and R. Jeanloz, Anomalous sound velocities in polycrystalline MgO under non-hydrostatic compression, Geophys. Res. Lett. **38**, L03304 (2011).

[13] O. V. Fat'yanov and P. D. Asimow, MgO melting curve constraints from shock temperature and rarefaction overtake measurements in samples preheated to 2300 K, J. Phys.: Conf. Ser. **500**, 062003 (2014).

[14] O. V. Fat'yanov and P. D. Asimow, Melting of B1-phase MgO from simultaneous true radiative shock temperature and

sound speed measurements to 250 GPa on samples preheated to 2300 K, J. Geophys. Res. **129**, e2024JB029137 (2024).
[15] J. M. Brown and T. J. Shankland, Thermodynamic parameters in the Earth as determined from seismic profiles, Geophys. J. Int. **66**, 579 (1981).
[16] Edited by J. R. Asay and M. Shahinpoor, *High-Pressure Shock Compression of Solids* (Springer, New York, NY, 1993).
[17] T. S. Duffy and T. J. Ahrens, Compressional sound velocity, equation of state, and constitutive response of shock-compressed magnesium oxide, J. Geophys. Res. **100**, 529 (1995).
[18] C. T. Seagle and A. J. Porwitzky, Shock-ramp compression of tin near the melt line, AIP Conf. Proc. **1979**, 040005 (2018).
[19] C. T. Seagle, J.-P. Davis, and M. D. Knudson, Mechanical response of lithium fluoride under off-principal dynamic shock-ramp loading, J. Appl. Phys. **120**, 165902 (2016).
[20] D. E. Fratanduono, M. Millot, D. G. Braun, S. J. Ali, A. Fernandez-Pañella, C. T. Seagle, J.-P. Davis, J. L. Brown, Y. Akahama, R. G. Kraus, M. C. Marshall, R. F. Smith, E. F. O'Bannon, J. M. McNaney, and J. H. Eggert, Establishing gold and platinum standards to 1 terapascal using shockless compression, Science **372**, 1063 (2021).
[21] J.-P. Davis, M. D. Knudson, L. Shulenburger, and S. D. Crockett, Mechanical and optical response of [100] lithium fluoride to multi-megabar dynamic pressures, J. Appl. Phys. **120**, 165901 (2016).
[22] J.-P. Davis, J. L. Brown, M. D. Knudson, and R. W. Lemke, Analysis of shockless dynamic compression data on solids to multi-megabar pressures: Application to tantalum, J. Appl. Phys. **116**, 204903 (2014).
[23] R. G. Kraus, J.-P. Davis, C. T. Seagle, D. E. Fratanduono, D. C. Swift, J. L. Brown, and J. H. Eggert, Dynamic compression of copper to over 450 GPa: A high-pressure standard, Phys. Rev. B **93**, 134105 (2016).
[24] S. Root, J. P. Townsend, and M. D. Knudson, Shock compression of fused silica: An impedance matching standard, J. Appl. Phys. **126**, 165901 (2019).
[25] F. Coppari, R. F. Smith, J. H. Eggert, J. Wang, J. R. Rygg, A. Lazicki, J. A. Hawreliak, G. W. Collins, and T. S. Duffy, Experimental evidence for a phase transition in magnesium oxide at exoplanet pressures, Nat. Geosci. **6**, 926 (2013).
[26] J. Wang, R. F. Smith, F. Coppari, J. H. Eggert, T. R. Boehly, G. W. Collins, and T. S. Duffy, Ramp compression of magnesium oxide to 234 GPa, J. Phys.: Conf. Ser. **500**, 062002 (2014).
[27] F. González-Cataldo, B. K. Godwal, K. Driver, R. Jeanloz, and B. Militzer, Model of ramp compression of diamond from *ab initio* simulations, Phys. Rev. B **104**, 134104 (2021).
[28] S. C. Grant, T. Ao, C. T. Seagle, A. J. Porwitzky, J.-P. Davis, K. R. Cochrane, D. H. Dolan, J.-F. Lin, T. Ditmire, and A. C. Bernstein, Equation of state measurements on iron near the melting curve at planetary core conditions by shock and ramp compressions, J. Geophys. Res. **126**, e2020JB020008 (2021).
[29] B. T. Hutsel, P. A. Corcoran, M. E. Cuneo, M. R. Gomez, M. H. Hess, D. D. Hinshelwood, C. A. Jennings, G. R. Laity, D. C. Lamppa, R. D. McBride, J. K. Moore, A. Myers, D. V. Rose, S. A. Slutz, W. A. Stygar, E. M. Waisman, D. R. Welch, and B. A. Whitney, Transmission-line-circuit model of an 85-TW, 25-MA pulsed-power accelerator, Phys. Rev. Accel. Beams **21**, 030401 (2018).
[30] R. W. Lemke, M. D. Knudson, and J.-P. Davis, Magnetically driven hyper-velocity launch capability at the Sandia Z accelerator, Int. J. Impact Eng. **38**, 480 (2011).
[31] M. Li and A. K. McNamara, The influence of deep mantle compositional heterogeneity on Earth's thermal evolution, Earth Planet. Sci. Lett. **500**, 86 (2018).
[32] B. A. Buffett, The thermal state of Earth's core, Science **299**, 1675 (2003).
[33] K. Hirose, G. Morard, R. Sinmyo, K. Umemoto, J. Hernlund, G. Helffrich, and S. Labrosse, Crystallization of silicon dioxide and compositional evolution of the Earth's core, Nature (London) **543**, 99 (2017).
[34] S. Root, L. Shulenburger, R. W. Lemke, D. H. Dolan, T. R. Mattsson, and M. P. Desjarlais, Shock response and phase transitions of MgO at planetary impact conditions, Phys. Rev. Lett. **115**, 198501 (2015).
[35] The temperature of the geotherm is conventionally defined as the temperature at 23 GPa (approximately 660 km depth on Earth). So a "1900 K" geotherm is the adiabat for which T = 1900 K where P = 23 GPa.
[36] See Supplemental Material at http://link.aps.org/supplemental/10.1103/x7x6-16cs for further descriptions of experimental and theory details, which includes Refs. [68,69].
[37] L. M. Barker and R. E. Hollenbach, Laser interferometer for measuring high velocities of any reflecting surface, J. Appl. Phys. **43**, 4669 (1972).
[38] O. T. Strand, D. R. Goosman, C. Martinez, T. L. Whitworth, and W. W. Kuhlow, Compact system for high-speed velocimetry using heterodyne techniques, Rev. Sci. Instrum. **77**, 083108 (2006).
[39] J.-P. Davis and J. L. Brown, Quantifying uncertainty in analysis of shockless dynamic compression experiments on platinum. I. Inverse Lagrangian analysis, J. Appl. Phys. **134**, 235901 (2023).
[40] S. D. Rothman, S. J. Ali, J. L. Brown, J. H. Eggert, and C. T. Seagle, Shock-ramp analysis test problem, J. Appl. Phys. **129**, 185901 (2021).
[41] J. L. Brown, J.-P. Davis, J. D. Tucker, G. Huerta, and K. W. Shuler, Quantifying uncertainty in analysis of shockless dynamic compression experiments on platinum. II. Bayesian model calibration, J. Appl. Phys. **134**, 235902 (2023).
[42] G. Kresse and J. Hafner, *Ab initio* molecular-dynamics simulation of the liquid-metal–amorphous-semiconductor transition in germanium, Phys. Rev. B **49**, 14251 (1994).
[43] G. Kresse and J. Furthmüller, Efficiency of *ab-initio* total energy calculations for metals and semiconductors using a plane-wave basis set, Comput. Mater. Sci. **6**, 15 (1996).
[44] G. Kresse and J. Furthmüller, Efficient iterative schemes for *ab initio* total-energy calculations using a plane-wave basis set, Phys. Rev. B **54**, 11169 (1996).
[45] J. P. Perdew, K. Burke, and M. Ernzerhof, Generalized gradient approximation made simple, Phys. Rev. Lett. **77**, 3865 (1996).
[46] G. Prandini, A. Marrazzo, I. E. Castelli, N. Mounet, and N. Marzari, Precision and efficiency in solid-state pseudopotential calculations, npj Comput. Mater. **4**, 72 (2018).
[47] G. Kresse and J. Hafner, Norm-conserving and ultrasoft pseudopotentials for first-row and transition elements, J. Phys. Condens. Matter **6**, 8245 (1994).
[48] G. Kresse and D. Joubert, From ultrasoft pseudopotentials to the projector augmented-wave method, Phys. Rev. B **59**, 1758 (1999).

[49] N. D. Mermin, Thermal properties of the inhomogeneous electron gas, Phys. Rev. **137**, A1441 (1965).

[50] Y. Fei, Effects of temperature and composition on the bulk modulus of (Mg,Fe)O, Am. Mineral. **84**, 272 (1999).

[51] J. Kim *et al.*, QMCPACK: An open source *ab initio* quantum Monte Carlo package for the electronic structure of atoms, molecules and solids, J. Phys. Condens. Matter **30**, 195901 (2018).

[52] J. P. Townsend, S. D. Pineda Flores, R. C. Clay, T. R. Mattsson, E. Neuscamman, L. Zhao, R. E. Cohen, and L. Shulenburger, Starting-point-independent quantum Monte Carlo calculations of iron oxide, Phys. Rev. B **102**, 155151 (2020).

[53] P. Giannozzi *et al.*, QUANTUM ESPRESSO: A modular and open-source software project for quantum simulations of materials, J. Phys. Condens. Matter **21**, 395502 (2009).

[54] P. Giannozzi *et al.*, Advanced capabilities for materials modelling with QUANTUM ESPRESSO, J. Phys. Condens. Matter **29**, 465901 (2017).

[55] M. C. Bennett, C. A. Melton, A. Annaberdiyev, G. Wang, L. Shulenburger, and L. Mitas, A new generation of effective core potentials for correlated calculations, J. Chem. Phys. **147**, 224106 (2017).

[56] M. C. Bennett, G. Wang, A. Annaberdiyev, C. A. Melton, L. Shulenburger, and L. Mitas, A new generation of effective core potentials from correlated calculations: 2nd row elements, J. Chem. Phys. **149**, 104108 (2018).

[57] M. Casula, S. Moroni, S. Sorella, and C. Filippi, Size-consistent variational approaches to nonlocal pseudopotentials: Standard and lattice regularized diffusion Monte Carlo methods revisited, J. Chem. Phys. **132**, 154113 (2010).

[58] Y. Fei, C. T. Seagle, J. P. Townsend, C. A. McCoy, A. Boujibar, P. Driscoll, L. Shulenburger, and M. D. Furnish, Melting and density of $MgSiO_3$ determined by shock compression of bridgmanite to 1254 GPa, Nat. Commun. **12**, 876 (2021).

[59] S. Root, J. P. Townsend, E. Davies, R. W. Lemke, D. E. Bliss, D. E. Fratanduono, R. G. Kraus, M. Millot, D. K. Spaulding, L. Shulenburger, S. T. Stewart, and S. B. Jacobsen, The principal Hugoniot of forsterite to 950 GPa, Geophys. Res. Lett. **45**, 3865 (2018).

[60] P. F. Weck, J. P. Townsend, K. R. Cochrane, S. D. Crockett, and N. W. Moore, Shock compression of niobium from first-principles, J. Appl. Phys. **125**, 245905 (2019).

[61] P. F. Weck, K. R. Cochrane, S. Root, J. M. D. Lane, L. Shulenburger, J. H. Carpenter, T. Sjostrom, T. R. Mattsson, and T. J. Vogler, Shock compression of strongly correlated oxides: A liquid-regime equation of state for cerium (IV) oxide, Phys. Rev. B **97**, 125106 (2018).

[62] C. Meade and R. Jeanloz, Yield strength of MgO to 40 GPa, J. Geophys. Res. **93**, 3261 (1988).

[63] M. B. Prime, S. J. Fensin, D. R. Jones, J. W. Dyer, and D. T. Martinez, Multiscale Richtmyer-Meshkov instability experiments to isolate the strain rate dependence of strength, Phys. Rev. E **109**, 015002 (2024).

[64] M. S. Vassiliou and T. J. Ahrens, Hugoniot equation of state of periclase to 200 GPa, Geophys. Res. Lett. **8**, 729 (1981).

[65] S. P. Marsh, *LASL Shock Hugoniot Data* (University of California Press, Berkeley, CA, 1980).

[66] G. F. Davies and T. J. Ahrens, Measurement of elastic velocities of MgO under shock compression to 500 kilobars, J. Geophys. Res. **78**, 7596 (1973).

[67] H. J. Bausch, J. P. Townsend, J.-P. Davis, S. Duwal, C. T. Seagle, T. M. Abbott, A. N. Clark, and S. D. Jacobsen, Direct sound speed measurements of MgO along planetary adiabats up to 400 GPa using shock-ramp compression [Dataset], Zenodo, 2026, doi: 10.5281/zenodo.23404812.

[68] K. Tomlinson, C. T. Seagle, H. Huang, G. E. Smith, J. L. Taylor, and R. R. Paguio, Enhanced dual confocal measurement system, Fusion Sci. Technol. **73**, 139 (2018).

[69] Y. Tange, Y. Nishihara, and T. Tsuchiya, Unified analyses for *P-V-T* equation of state of MgO: A solution for pressure-scale problems in high *P-T* experiments, J. Geophys. Res. **114**, B03208 (2009).

[70] C.-S. Zha, H.-k. Mao, and R. J. Hemley, Elasticity of MgO and a primary pressure scale to 55 GPa, Proc. Natl. Acad. Sci. USA **97**, 13494 (2000).